Engineering Analysis with Boundary Elements 119 (2020) 119–132

Contents lists available at ScienceDirect

Engineering Analysis with Boundary Elements

journal homepage: www.elsevier.com/locate/enganabound

A novel two-way coupling *model* for Euler-Lagrange simulations of multiphase flow

O. Verhnjak[a,*], M. Hriberšek[a], P. Steinmann[b], J. Ravnik[a]

[a] Faculty of Mechanical Engineering, University of Maribor, Smetanova ulica 17, SI-2000 Maribor, Slovenia
[b] Chair of Applied Mechanics, Friedrich-Alexander Universität Erlangen-Nürnberg, Paul-Gordan-Str. 3, Erlangen D-91052, Germany

ARTICLE INFO

Keywords:
Boundary element method
Particle-in-cell
Critical distance
Point-wise particles
Multiphase flows

ABSTRACT

We propose a novel approach for two-way coupled simulations of multiphase flows within an Eulerian-Lagrange framework. Lagrangian particles are commonly approximated as point sources of either energy, mass or momentum. To introduce them into the Eulerian computation of the fluid flow, an approximation of the Dirac delta function has to be made. By resorting to the Boundary Element Method (BEM) based computation of fluid flow, it is possible to implement the point source concept without any numerical approximation by simply taking advantage of the properties of the fundamental solution present in BEM. However, singularity issues occur in the close vicinity of the mesh nodes. To remedy this effect, the particle-in-cell (PIC) method is used. We present a novel hybrid BEM-PIC two-way coupling algorithm and show that the proposed BEM-PIC model gives superior results compared to a standard PIC implementation. We introduce a critical distance to separate the domain, where the BEM model can be used and the domain, where the PIC model should be used. The results show that the BEM model can be used in about 97% – 99% of the domain depending on the mesh used. We provide a criterion for estimating the critical distance within the novel hybrid BEM-PIC two-way coupling algorithm.

1. Introduction

Multiphase flows are one of the central topics in process technology. Its two main aspects are either separation or, in the contrary, the mixing of two pure substances in an as homogeneous as possible fashion. Research of the topic has led to different applications ranging from cyclonic separators and dust collectors to fluidized beds [1,2]. Multiphase flows generally consist of all three known phases: gaseous, liquid and solid [3], but it is often desirable to reduce the number of phases in the mixture. Thus, the phenomenon is further reduced to three types of two-phase flows: liquid-solid, gas-liquid, liquid-gas, which are easier to model. Generally objects in nature move due to force systems acting on them. Understanding these forces plays a central role in the mathematical description of the motion of things. However, due to the inability to describe all types of force systems, the chosen phenomenon has to be simplified in order to be described mathematically. The simplification of the force systems in two-phase flows is most significant in the case of one-way coupled flow, where only the force in the direction from the carrier phase to the particulate phase is accounted for [4]. Taking into account the mutual interaction between the two phases is called two-way coupling. The most precise force model is four-way coupling, since it adds the computation of particle collisions [5]. According to the volume ratio of both phases there are dense and dilute flows. The volume ratio decides which forces play the most significant role. The most important forces for dilute flows are interaction forces between the two phases, whereas for dense particulate flows the main flow characteristics are defined by the particle collisions. Dense particulate flows are mainly modeled in the Euler coordinate description and are numerically based on volume averaging [6]. Accounting for the given simplifications the authors have derived the VANS equations, which are able to solve two-way coupled problems [7,8] and four-way coupled problems [9]. While it is possible to solve dense flows using the Euler-Lagrange method, it is deemed as numerically too costly, because of the multitude of particles that has to be resolved [10].

There are several approaches to describe dilute disperse flows. They differ in the required computational cost and the number of physical quantities accounted for. The equilibrium Eulerian approach is discussed in [11]. It assumes particles of small size and mass, leading to Stokes numbers much smaller than one ($St < < 1$). Thus, the velocity of the particles is fully dependent on the carrier phase flow field. The dispersed phase can also be represented as a continuum, which was first described by Crowe [12] and later improved by Fevrier [13]. They proposed that conservation equations should be solved for each of the phases, with momentum and energy exchange between the phases taken into ac-

* Corresponding author.
E-mail addresses: ozbej.verhnjak@gmail.com (O. Verhnjak), matjaz.hribersek@um.si (M. Hriberšek), paul.steinmann@fau.de (P. Steinmann), jure.ravnik@um.si (J. Ravnik).

https://doi.org/10.1016/j.enganabound.2020.07.012
Received 27 March 2020; Received in revised form 1 July 2020; Accepted 15 July 2020

count as source and sink terms. Numerical investigations have shown that the most important advantage of the method is its ability to compute even bigger particles. The method most used is the Euler-Lagrange method [14,15], wherein undisturbed flow in the vicinity of the particle is assured, which is computed directly without using turbulent models. While the fluid flow is computed using the Eulerian approach, the Lagrangian approach is used to resolve the particulate phase. The motion of the particles is calculated by the direct use of Newton's laws for the motion or, recently, with the discrete element method (DEM) [16]. The latter enables the computation of many particles. The usefulness of the Euler-Lagrange method for two-way coupled flows depends on the accuracy of the interphase momentum and energy transfer between particles and mesh vertices. The interphase momentum and energy transfer is computed in two steps. Firstly, we have to calculate the forces and heat transfer terms acting on the particulate phase. This requires the calculation of the fluid velocity at the particle's locations and at the grid points. Additionally, the temperatures at the same locations have to be defined in order to resolve the energy transfer. In the second step the interphase exchange is calculated using forces and energy sources or sinks previously computed. The Euler-Lagrange methodology, however, has been mainly applied only to two-phase flows, for which the particles are of sizes smaller than the Eulerian grid and for which the volume fraction of the particles is reasonably small. The first crucial step in a two-way coupled Euler-Lagrange methodology is the computation of the velocity and the temperature at the particle's location as stated above. The accuracy of the computed velocity and temperature has a substantial effect on the computation of the forces and the heat transfer. Most of the models to compute the drag force and heat transfer assume an isolated particle, which is subjected to a uniform flow. This restriction allows the flow properties at the particle location to be computed as an interpolation of nearby grid points. The second crucial step is the computation of the particle's impact on the fluid flow. Different methods have been proposed on how to represent the particle's feedback force and energy to the Eulerian grid. The particle-in-cell method has been introduced by Evans and Harlow [17] and has been supplemented by Crowe [18]. The method is based on volume averaging across the computational cell, in which the particle is located. Whereas the biggest advantage of the method is its low computational cost, it has the disadvantage of not having a physical interpretation. The second disadvantage is the mesh size dependency [19]. In [20] the feedback to the fluid field is captured using Gaussian volume filtering. Recently, many attempts have been made to avoid the restriction on particles size, thus making their size comparable to that of the grid. As the grid size increases, the particle force and energy feedback become larger and tend to affect the local flow at the particle location, which leads to disturbed flow in the vicinity of the particle. The fluid velocity and temperature computed at the particles location are thus substantially different from the case of small particles. The force and heat transfer computed with the velocity and temperature of the undisturbed flow differ from the case of the disturbed flow. As the standard drag laws and heat transfer coefficient approximations assume undisturbed flow near the particles, and in order to avoid using the properties from the undisturbed flow, several approaches have been proposed to correct the flow properties [21–24].

The particle's feedback is projected to the Eulerian mesh using different mathematical approximations that try to approximate the point source without losing too much of its physical meaning. In this work we will pursue the computation of two-way coupling using the BEM. The same method will be used to compute the continuous phase. While applying the single domain BEM has the advantage of high resolution accuracy, it is also computationally very expensive, since the matrices obtained are full. There have been several attempts to reduce the computational cost using the subdomain BEM [25], which ameliorates the speed of the computation, because the solution leads to a sparse system of linear equations. A sparse system allows for fast algebraic operations and does not require a lot of storage as it is proven in [26]. Additionally, the method can be improved by applying the dual reciprocity method

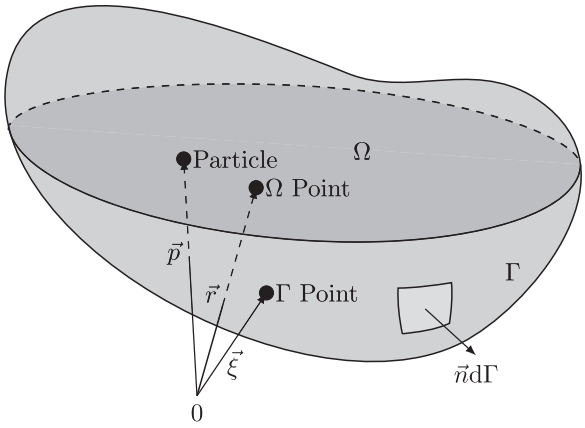

Fig. 1. The boundary Γ and domain Ω positions, which are denoted by $\vec{\xi}$ and $\vec{r}$ respectively, are being shown. The particle's position is represented by the vector $\vec{p}$.

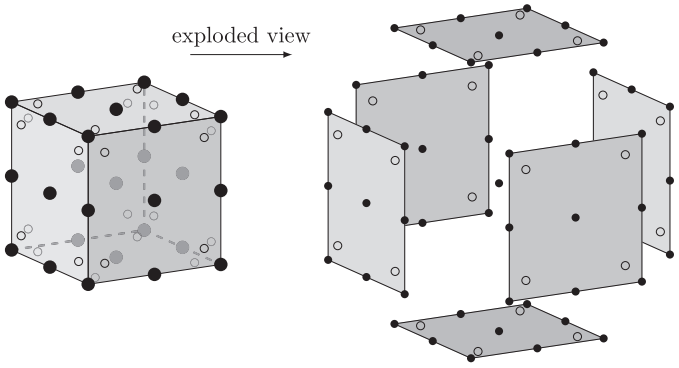

Fig. 2. Every domain element consists of 27 function nodes (filled circles) and 24 flux nodes (empty circles).

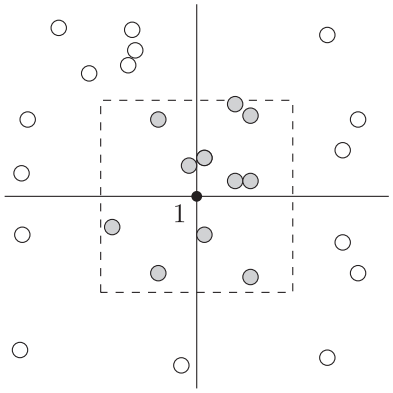

Fig. 3. The standard approach using PIC is to define a control volume around a node (node 1) and then finding all the particles inside the chosen control volume. The energy of all the particles is summed and projected to the node inside the control volume.

[27] or triple reciprocity method [28,29]. Another possibility is to use different approximations in order to reduce the matrix size [30]. It has been mentioned above that the feedback from the particles in a Eulerian grid is included as a source/sink term which, in the BEM context, can be applied directly, without any loss of accuracy of the point particle approximation [31]. The treatment of the point-wise sources with the BEM is especially simple, since in the integral forms of the energy and momentum transfer equations the effect of particles is implemented as a simple sum. An example of applying the single domain BEM for the

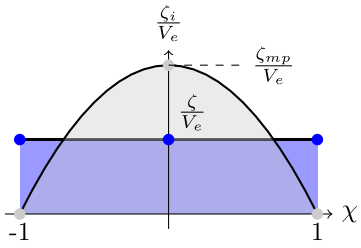

Fig. 4. In the case of linear interpolation inside the element (blue fill) every node is prescribed with the same contribution of the particle's energy source ζ, which is simply the particle's source divided by the volume of the element. The integration over the volume of the element returns the value of the particle's source. However, when quadratic interpolation is used (grey fill) the most straight forward implementation is to prescribe all the nodes, except the center node, with zero contribution of the particle's source. Again, the integration of the contribution over the element's volume must return the source ζ and in order to ensure that, the center node has to be prescribed with a modified energy source ζ_{mp}. (For interpretation of the references to colour in this figure legend, the reader is referred to the web version of this article.)

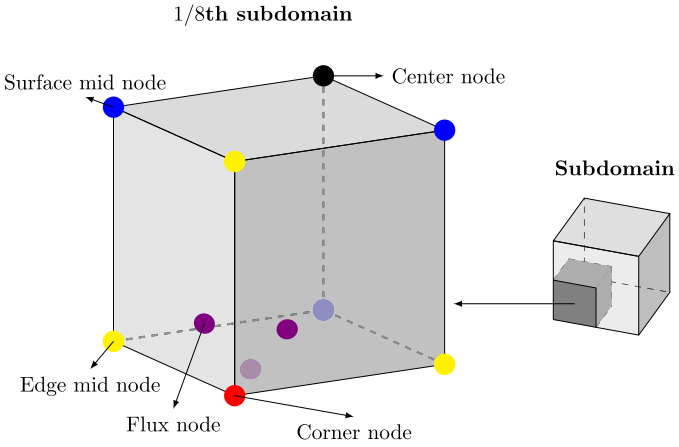

Fig. 5. The particle is located in the selected element within the cubic domain, whereby we use the symmetry property of the element to reduce the number of simulations required.

two-way coupled heat conduction in solid problems is given in [32]. However, the derivation of the BEM is based on the method of weighted residuals, where the fundamental solutions used have similar properties to the Dirac delta function, used in the point particle two-way coupling. The final integral equations are based on a fundamental solution, which is a solution of the chosen differential equation. Independently of the chosen solution, they are singular at the point, where the delta function is defined. The point of singularity is reached only in the case when two vertices or a vertex and a particle are too close. Because the single domain BEM has its mesh points only on the boundary surface, the potential for the fundamental solution to be singular is low due to the distance between the particle and the boundary surface. When the subdomain BEM is used, the boundaries of almost all subdomains lie in the domain. Thus, there exists a limit, where the particle can be located in the overall domain, if the singularity is to be avoided.

In this work we follow the above observations and address the two-way coupling of two-phase flows using the BEM to calculate continuous phase and either BEM or PIC as a coupling method. Mathematically correct way of introducing point particle source in the Eulerian mesh is by using Dirac delta function, whose drawback is its singularity property. The conventional coupling methods, e.g. PIC,avoid the Dirac delta function problem of the singularity by approximating the cell in which the particle is located as the particle itself. By making such an assumption, the overall accuracy of the two-way coupled computation is strongly dependent on the grid size. On the contrary, if the coupling is based on the Dirac delta function, the results of the coupling are grid independent. By using the BEM it is possible to distribute the source due to the presence of the particle to the grid element nodes without loss of accuracy. We can use the Dirac delta function sifting property to convert the volume integral into a sum. This represents an advantage over other methods, e.g. the finite element method, and is the main reason to use the BEM for the problem, even if other methods would be more suitable for the defined physical problem. However, because of the Dirac delta function, the function assigning the shares is singular in the distance between the node and the particle. The research we will pursue is connected with the definition of space in the domain, where the particle may be located in order to not mathematically influence the accuracy of the results. Additionally, we will propose an effective solution method to implement the novel hybrid BEM-PIC coupling algorithm.

2. Governing equations

As a model problem we consider heat diffusion from a point-wise particle with a constant heat source I^* in a stationary fluid. The heat is transferred to fluid in an isotropic manner, which, together with the assumption of the domain being unbounded, enables us to neglect the effect of natural convection. The chosen phenomenon is representative and the analytical solution in an unbounded domain is known. Let us consider a system with a non-inertial frame of reference at the position of the particle. In a fully resolved DNS analysis, the thermal boundary conditions would be known on the particle surface and the interphase energy exchange would be calculated appropriately. In the diffusion equation there would be no additional heat sources. In the case of Euler-Lagrange two-way coupling, however, no specific boundary conditions are applied on the particle surface. Instead, their feedback is incorporated into the Eulerian mesh with an additional source term. The heat diffusion equation then reads as:

$$\rho c_p \frac{\partial T^*}{\partial t^*} = k\nabla^2 T^* + I^*, \tag{1}$$

where T^* is the temperature, c_p is the specific heat, t^* is the time, k is the thermal conductivity and I^* $[W/m^3]$ is the energy source. The "*" denotes dimensional values. In our approach, the particles are point-wise (since this generally allows for the use of standard heat transfer coefficients developed for an isolated particle in a uniform flow). For the source we thus have:

$$I^* = \dot{Q}^* \delta(\vec{r}^*, \vec{p}^*), \tag{2}$$

where $\dot{Q}^*$ $[W]$ represents the thermal power, $\delta(\vec{r}^*, \vec{p}^*)$ $[1/m^3]$ is the Dirac delta function, $\vec{r}^*$ denotes the position vector and $\vec{p}^*$ represents the position of the particle. The delta function in (2) is a mathematically exact expression for the point-wise property of the particles. We can use a macroscopic approach instead, without using the delta function. The energy contribution of the particle is distributed over a small part of the entire domain expressed as

$$I^* = \frac{\dot{Q}^*}{V^*}, \tag{3}$$

where V^* is a small volume. The standard approach in the Euler-Lagrange methodology uses (3) for which the equation is never singular. Therefore, it is used as the basis for the derivation of the PIC method. The Dirac delta function in (2) suggests that the equation in this form is suitable for the application of Green's theorem.

The above equations are now non-dimensionalized via the following expressions:

$$\tau = \frac{\alpha t}{L^2}, \quad T = \frac{T^* - T_0^*}{\Delta T^*}, \quad \zeta = \frac{\dot{Q}^*}{k\Delta T^* L}, \quad \vec{r} = \frac{\vec{r}^*}{L}, \quad \vec{p} = \frac{\vec{p}^*}{L}, \quad V = \frac{V^*}{L^3},$$

where α is the thermal diffusivity, L is a characteristic dimension, T_0^* is the initial temperature, ΔT^* is the temperature difference between

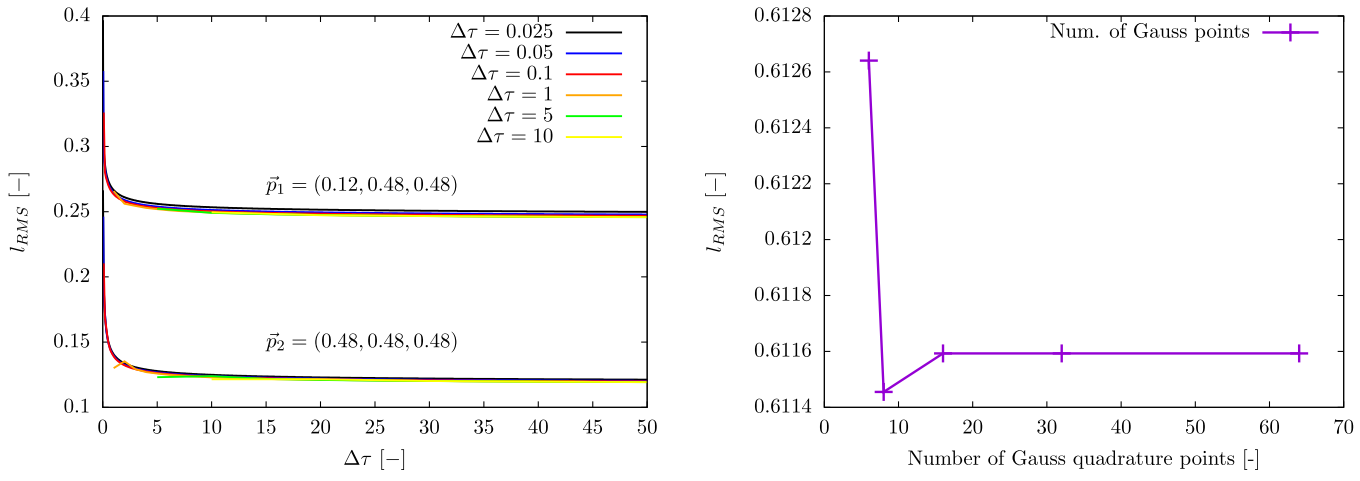

(a) $\Delta\tau$ influence (b) Gauss points

Fig. 6. (Left): the effect of $\Delta\tau$ on the simulation results. The integrals have been approximated using Gauss quadrature, for which the number of Gauss points has to be chosen. (Right): To avoid the unnecessary long integration times, we have made an analysis of how the number of Gaus points influences the results (panel 6b).

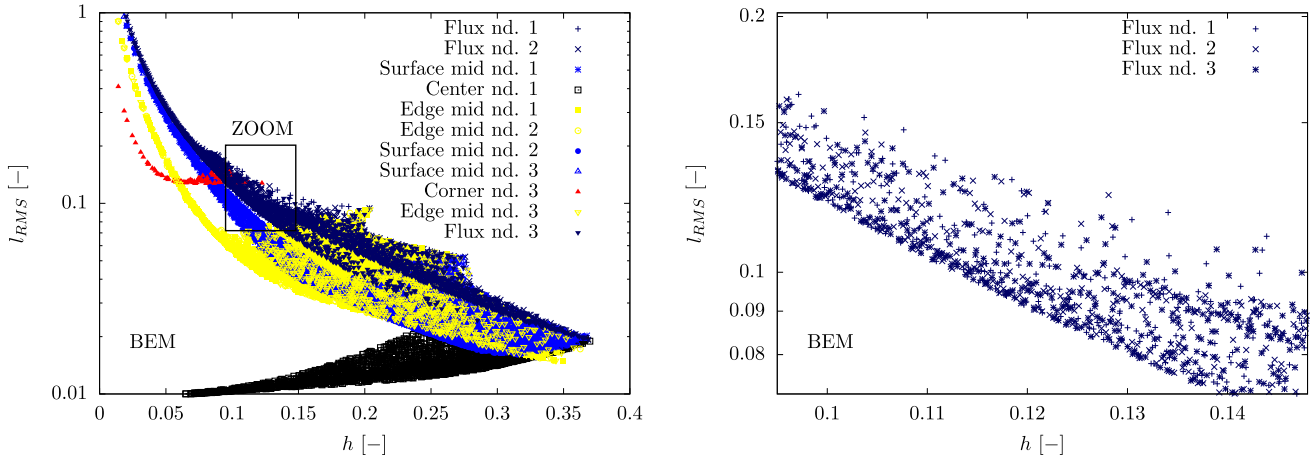

(a) BEM coupling - all nodes (b) BEM coupling - flux node group

Fig. 7. (Left) Every 5th particle's distance h vs. l_{RMS} is shown. (Right) As it is not clear that every type of source points has the same characteristics and also the l_{RMS} values for the same distance h, 7b shows the details for the points inside the black rectangle (only Flux nodes).

the initial temperature and the temperature after a very long time. Eq. (1) transforms into either of the following

$$\frac{\partial T}{\partial \tau} - \nabla^2 T = \sum_j \zeta \delta(\vec{r}, \vec{p}_j) \text{ or} \tag{4}$$

$$\frac{\partial T}{\partial \tau} - \nabla^2 T = \sum_j \frac{\zeta(\vec{p}_j)}{V}, \tag{5}$$

where we have used the delta function source representation (2) and the macroscopic source representation (3) to obtain the above equations. With $\zeta(\vec{p})$ in (5) the heat source is bound to the volume V. The summation terms in (4) and (5) considers each particle in the system.

3. Numerical method

We will now apply the subdomain BEM to solve the equations listed in the previous section. The subdomain BEM uses a domain decomposition approach to handle inhomogeneous PDEs and is used to solve either Eqs. (4) or (5).

3.1. BEM two-way coupling approach

Using the first and second Green's theorems, we obtain the integral form of Eq. (4) [33]:

$$c(\vec{\xi})T(\vec{\xi}) + \int_\Gamma T(\vec{r})\vec{q}^*(\vec{\xi},\vec{r})\cdot d\vec{\Gamma} = \int_\Gamma u^*(\vec{\xi},\vec{r})\vec{q}\cdot\vec{n}d\Gamma - \int_\Omega \frac{\partial T(\vec{r})}{\partial \tau} u^*(\vec{\xi},\vec{r})d\Omega + \int_\Omega \sum_j \zeta\delta(\vec{r},\vec{p}_j)u^*(\vec{\xi},\vec{r})d\Omega, \tag{6}$$

where $\vec{\xi}$ is the position vector of the source point, $u^*(\vec{\xi},\vec{r}) = \frac{1}{4\pi|\vec{\xi}-\vec{r}|}$ is the fundamental solution for the Laplace operator, $\vec{q}^*(\vec{\xi},\vec{r})$ is the gradient of the fundamental solution, $c(\vec{\xi})$ is the free term coefficient and $\vec{q} = \vec{\nabla}T$. For the given set of equations there exists a fundamental solution, which would enable the use of single-domain BEM as solution method and would be better applicable to the problem. However, the choice of the fundamental solution in this paper was due to the possible extension of the model to the full set of the Navier-Stokes equation in the future, for which no appropriate solutions exist. The boundary surface and the volume of the domain are denoted by Γ and Ω, respectively. The representation of the computational parameters is given in

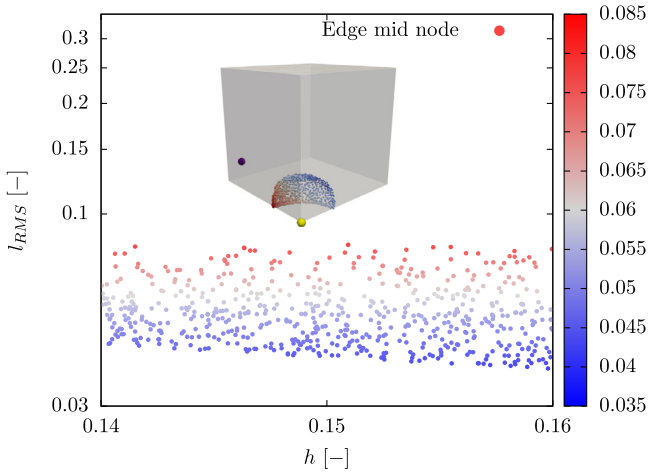

Fig. 8. The yellow point in the front of the inset panel is the edge mid source point around which are the particles with least distance inside the interval of [0.14,0.16]. Of these particles the ones whose next nearest point is the flux source point (purple color) have the highest *RMS* value. (For interpretation of the references to colour in this figure legend, the reader is referred to the web version of this article.)

Fig. 1. The time derivative is approximated using a second order accurate three-point finite difference scheme, which reads:

$$\frac{\partial T}{\partial \tau} = \beta_1 T^{n+1} - \beta_2 T^n + \beta_3 T^{n-1}, \tag{7}$$

where $\beta_1 = \frac{3}{2\Delta\tau}$, $\beta_2 = \frac{2}{\Delta\tau}$ and $\beta_3 = \frac{1}{2\Delta\tau}$, T^n and T^{n-1} define the temperature in the current and the previous time step, respectively. If we now consider the energy source term (last term on right hand side) in Eq. (6), we can use the Dirac delta function sifting property to rewrite the expression as:

$$\int_\Omega \sum_j \zeta \delta(\vec{r}, \vec{p}_j) u^*(\vec{\xi}, \vec{r}) \mathrm{d}\Omega = \sum_j \zeta u^*(\vec{\xi}, \vec{p}_j), \tag{8}$$

where the fundamental solution u^* is calculated as

$$u^*(\vec{\xi}, \vec{p}_j) = \frac{1}{4\pi|\vec{\xi} - \vec{p}_j|}. \tag{9}$$

The upper equation is singular for the distance $|\vec{\xi} - \vec{p}_j|$. In the manuscript we will not propose a solution of the singularity problem in direct meaning, but rather a workaround. We define a critical distance, i.e. a boundary line between the particle and the mesh node, which serves as a deciding factor for the coupling method. The singularity only affects the calculation if the distance between the particle and mesh node is smaller than the critical distance. Therefore, if the critical distance is not crossed, the BEM method can be used to couple the particle sources. If the distance between the particle and mesh node is smaller than the critical distance, we avoid the singularity problem by using the PIC coupling method presented in the following chapter.

Equation (6) contains the boundary values of the function T and the boundary values of the normal flux $q = \vec{q} \cdot \vec{n}$. To use (6), time-dependent boundary conditions for the function or for the flux have to be known. The integral equation consists of boundary and domain integrals. Since the governing Eq. (6) contains domain integrals, we use the domain decomposition approach to avoid large full matrices. Therefore, the discretization of the entire domain is necessary. We consider each mesh element as a separate sub-domain. The domain is split using hexahedral elements [34]: $\Omega = \sum_e \Omega_e$. The sides of the elements consist of boundary elements $\Gamma = \sum_b \Gamma_b$. Using the given mesh set up, we can rewrite Eq. (6) as:

$$\begin{aligned} c(\vec{\xi})T(\vec{\xi}) + \sum_b \int_{\Gamma_b} T(\vec{r})\vec{q}^*(\vec{\xi}, \vec{r}) \cdot \mathrm{d}\vec{\Gamma} \\ = \sum_b \int_{\Gamma_b} u^*(\vec{\xi}, \vec{r})\vec{q} \cdot \vec{n}\mathrm{d}\Gamma - \sum_e \int_{\Omega_e} [\beta_1 \mathrm{T} - \beta_2 \mathrm{T}^n + \beta_3 \mathrm{T}^{n-1}] \mathrm{u}^*(\vec{\xi}, \vec{\mathrm{r}})\mathrm{d}\Omega \\ + \sum_j \zeta u^*(\vec{\xi}, \vec{p}_j), \end{aligned} \tag{10}$$

where we have already accounted for the approximation of the time derivative given in (7) and for the modified form of the energy source. The domain elements have 27 nodes with which a continuous quadratic interpolation is performed. The interpolation is performed with the Lagrange interpolation functions Φ_i. Each boundary element Γ_b has nine nodes, which allow for the interpolation of a function using the interpolation function φ_i. Additionally, there are four nodes on each boundary element Γ_b for the discontinuous interpolation of the flux. Locations of these flux nodes are not random but are constant with the following coordinates in the local coordinate system of every boundary element $[-1, 1]^2$: (-0.75, 0.75), (-0.75, -0.75), (0.75, -0.75), (0.75, 0.75). The shape function allowing for the interpolation across the boundary

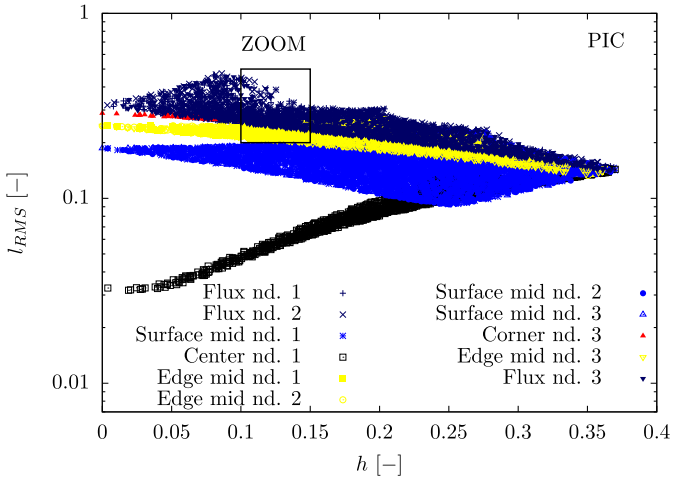

(a) PIC coupling all nodes

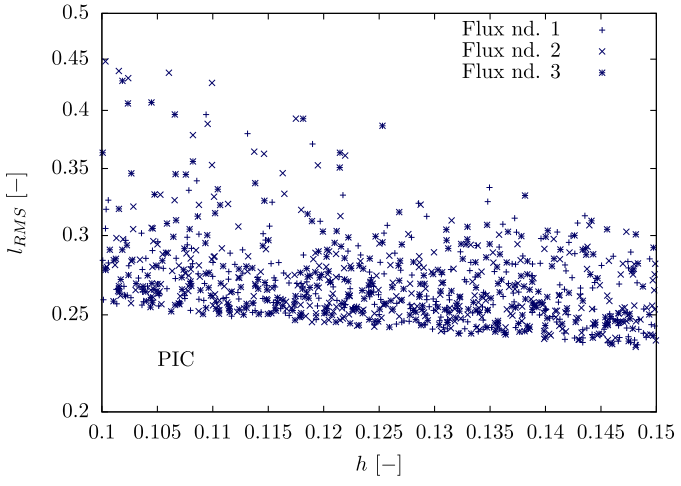

(b) PIC coupling flux node group

Fig. 9. The results of the simulations using PIC do not change, if the particles are located in the same element. However, because of the definition in Eq. (21), the resulting l_{RMS} will vary also for the PIC method as represented in the 9a. Moreover, the simulations are done using the same particle's locations as with the BEM two-way coupling algorithm and as a result, the particles may be distributed into the same node type groups as in the case of BEM two-way coupling.

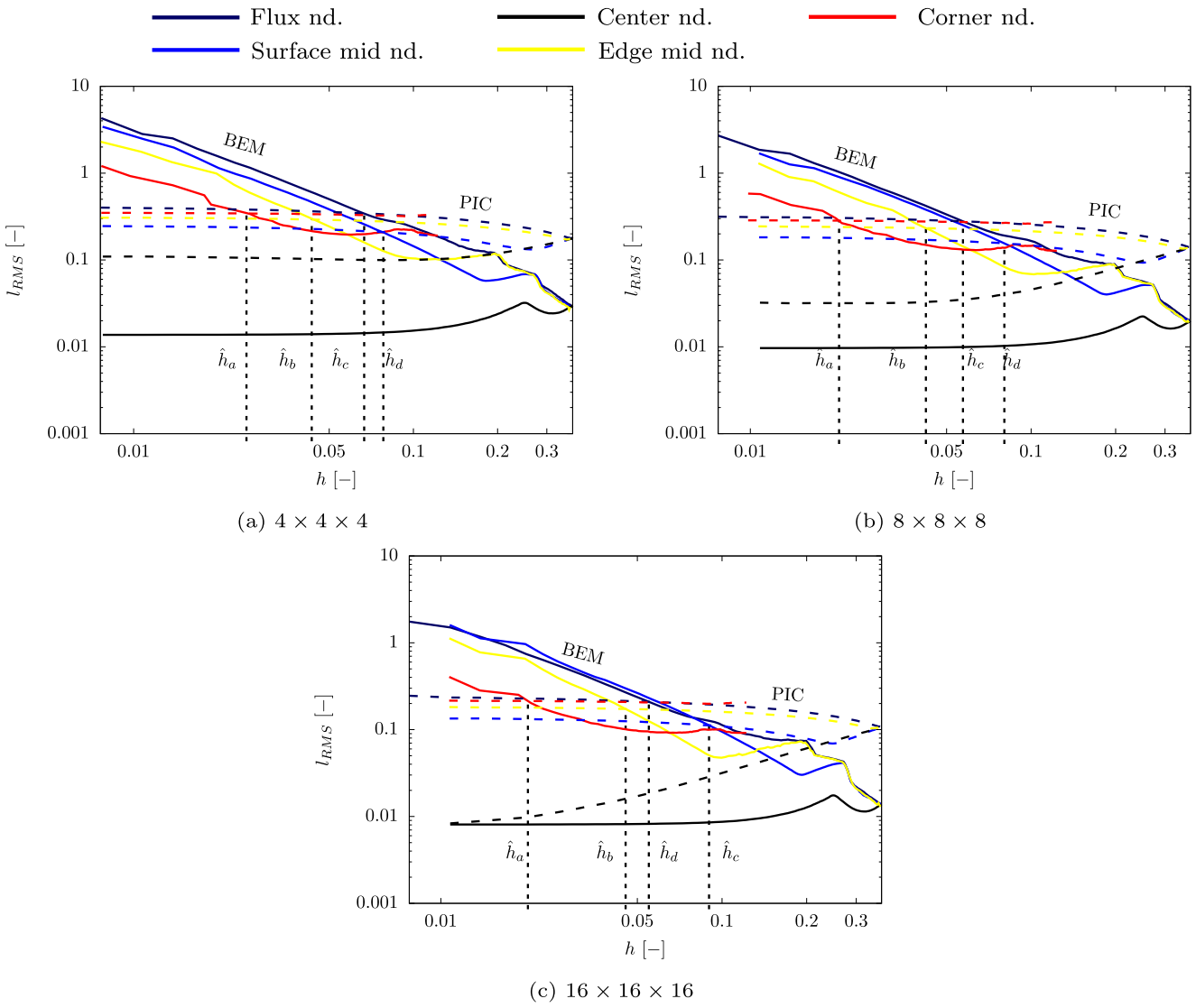

Fig. 10. l_{RMS} for a representative of each mesh node group is shown. The accuracy of the BEM two-way coupling algorithm depends largely on the distance between the particle and the mesh node, so worst case simulations are taken into account when preparing the figure. We filter the l_{RMS} of the BEM two-way coupled simulations and the PIC simulations with the lowest l_{RMS}. For each mesh node group we define a critical distance $\hat{h}$, which is the minimum distance between the particle and nearest node if the simulation is to be calculated with the BEM two-way coupling algorithm. The critical distance can be determined by equating the BEM and the PIC two-way coupling l_{RMS}. The BEM two-way coupled simulations are shown with a full line, while the dotted line represents PIC two-way coupled simulations.

element is represented by ϕ_i. The arrangement of the boundary nodes is shown in Fig. 2. Using the given shape functions, we are able to interpolate a function T over a boundary element as $T = \sum \varphi_i T_i$ and in the domain as $T = \sum \Phi_i T_i$. The flux interpolation proceeds over the boundary element as $q = \sum \phi_i q_i$.

We can now rewrite Eq. (10):

$$c(\vec{\xi})T(\vec{\xi}) + \sum_b \sum_i T_{b,i}(\vec{r}) \int_{\Gamma_b} \varphi_i \vec{q}^*(\vec{\xi},\vec{r}) \cdot \mathrm{d}\vec{\Gamma} = \sum_b \sum_i q_{b,i} \int_{\Gamma_b} \phi_i u^*(\vec{\xi},\vec{r}) \mathrm{d}\Gamma - \sum_e \sum_i [\beta_1 T_{e,i} - \beta_2 T^n_{e,i} + \beta_3 T^{n-1}_{e,i}] \int_{\Omega_e} \Phi_i u^*(\vec{\xi},\vec{r}) \mathrm{d}\Omega + \sum_j \zeta u^*(\vec{\xi},\vec{p}_j). \tag{11}$$

The integrals in the previous equation depend solely on the fundamental solution and the mesh shape. For a chosen source collocation point $\vec{\xi}$, they can be calculated in advance and will not change through the simulation. Integrals are approximated by Gaussian quadrature via the weighted summation of 8 Gaussian points in a local coordinate system. Considering a known solution of the rigid body motion, $T = 1, \quad q = 0$, we can indirectly calculate the singular integrals. If the source point is on the boundary, $c = 0.5$, and if it is within the domain, it has the value $c = 1$. In each sub-domain, the source point sweeps over all function and flux nodes. We calculate the integrals and group them into matrices:

$$[H] = \int_\Gamma \varphi_i \vec{q}^* \cdot \vec{\Gamma}, \quad [G] = \int_\Gamma \phi u^* \mathrm{d}\Gamma, \quad [\mathrm{B}] = \int_\Omega \Phi_\mathrm{i} \mathrm{u}^* \mathrm{d}\Omega. \tag{12}$$

The square brackets denote integral matrices. With curly brackets denoting vectors of nodal values of functions, the discrete version of (11) reads:

$$[H]\{T\} = [G]\{q\} - [B]\{\beta_1 T - \beta_2 T^n + \beta_3 T^{n-1}\} + \sum_j \zeta u^*\left(\vec{\xi}, \vec{p}_j\right). \tag{13}$$

Further details regarding the numerical implementation can be found in [26].

As the particle approaches the source point, we expect the last term on the right hand side of Eq. (12) to be very large, with an infinite value

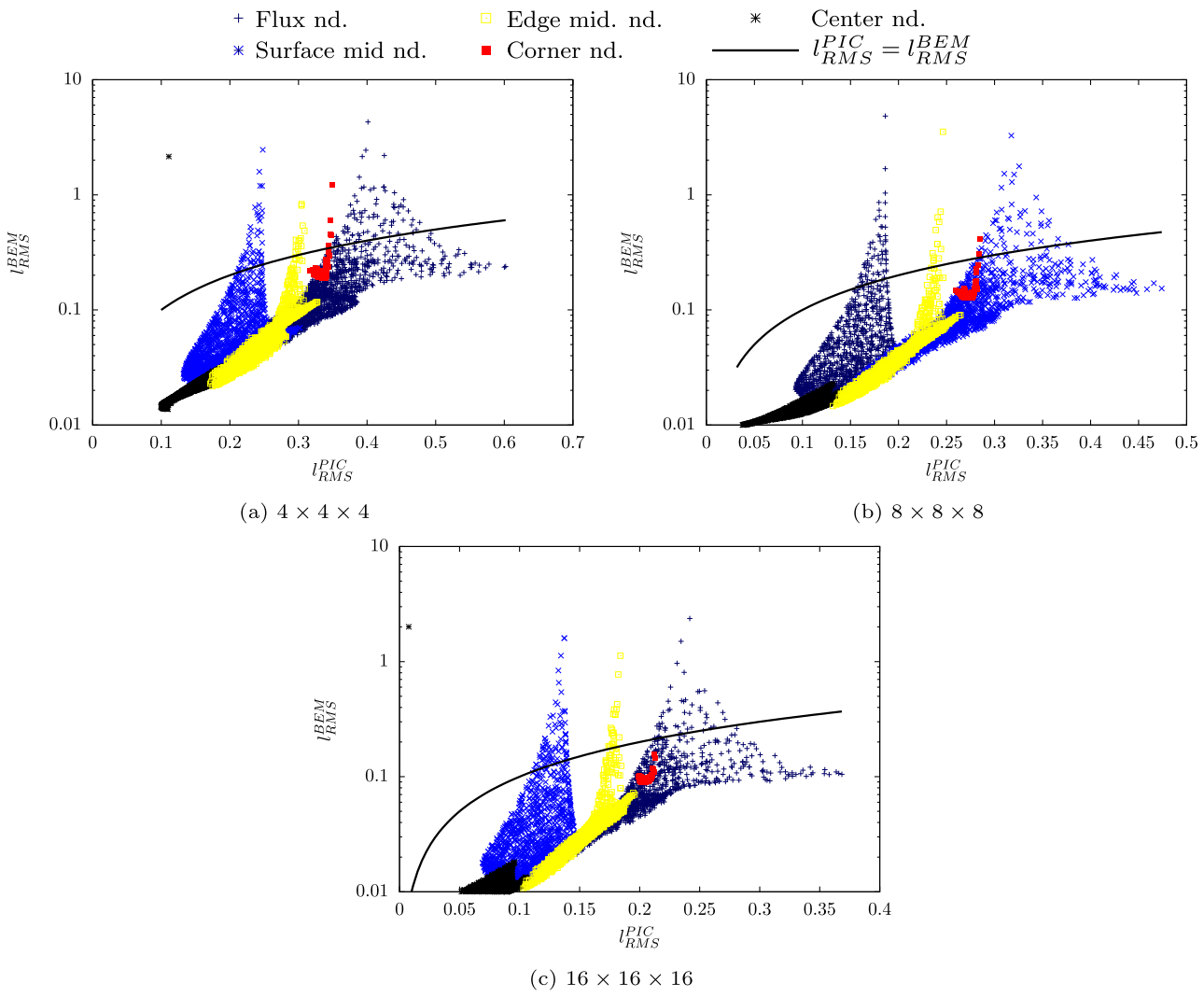

Fig. 11. The phase diagrams show the relationship between the results obtained by PIC two-way coupling and these obtained using BEM two-way coupling. The black line represents a border where PIC two-way coupling l_{RMS} equals BEM two-way coupling l_{RMS}.

at the location of the source point. The $u^*(\vec{\xi}, \vec{p}_j)$ in (12) is used as a filter, which assigns the share of particle's heat source onto every node in the Eulerian mesh according to the distance between the particle and the given node. However, when the particle's and the node's positions are identical, the node is deemed to be inside the particle, which is not valid. Additionally, due to singular nature of u^*, the small distance between particle and node has a negative effect on the accuracy of (11). Thus, we introduce a critical distance which, when crossed, causes the accuracy of (11) to be poor.

3.2. PIC two-way coupling approach

Historically, the PIC method was mostly used as a mathematical model to incorporate particle feedback into the Eulerian mesh. The approach is based on the definition of a control volume V in which the particle is located and over which the particle energy source is distributed (Fig. 3). Let us define a mesh element in which the particle is located as this control volume. Then the volume fraction V in (14) is the volume of the mesh element. Thus Eq. (5) can be used directly for the implementation of PIC. First we write the integral form of Eq. (5):

$$c(\vec{\xi})T(\vec{\xi}) + \int_\Gamma T(\vec{r})\vec{q}^*(\vec{\xi},\vec{r})\cdot \mathrm{d}\vec{\Gamma} = \int_\Gamma u^*(\vec{\xi},\vec{r})\vec{q}\cdot \mathrm{d}\vec{\Gamma} - \int_\Omega \frac{\partial T(\vec{r})}{\partial \tau} u^*(\vec{\xi},\vec{r})\mathrm{d}\Omega + \sum_j \frac{1}{V}\int_\Omega \zeta(\vec{p}_j)u^*(\vec{\xi},\vec{r})\mathrm{d}\Omega. \quad (14)$$

We use the same approximation as in Section 3.1 regarding the time derivative. Also, the elements have the same number of nodes, and we use the same shape functions to interpolate the function values. Additionally, we use the Φ_i shape functions to interpolate the energy source over the element domain $\zeta = \sum \Phi_i \zeta_i$. With these preliminaries we can write the discrete version of (14):

$$\begin{aligned} c(\vec{\xi})T(\vec{\xi}) + \sum_b \sum_i T_{b,i}(\vec{r}) \int_{\Gamma_b} \varphi_i \vec{q}^*(\vec{\xi},\vec{r})\cdot \mathrm{d}\vec{\Gamma} \\ = \sum_b \sum_i q_{b,i} \int_{\Gamma_b} \phi_i u^*(\vec{\xi},\vec{r})\mathrm{d}\Gamma - \sum_e \sum_i [\beta_1 T_{e,i} \\ - \beta_2 T^n_{e,i} + \beta_3 T^{n-1}_{e,i}] \int_{\Omega_e} \Phi_i u^*(\vec{\xi},\vec{r})\mathrm{d}\Omega + \sum_e \sum_i \sum_j \frac{1}{V_e}\int_\Omega \Phi_i \zeta_{e,i} u^*(\vec{\xi},\vec{r})\mathrm{d}\Omega. \end{aligned} \quad (15)$$

A more precise representation of the last energy source term is needed at this point.

The heat source introduced by the particle is distributed over only one element, which means that this term is zero for all elements except the one in which the particle is located. Furthermore, since quadratic interpolation has been chosen as the interpolation function for the in-

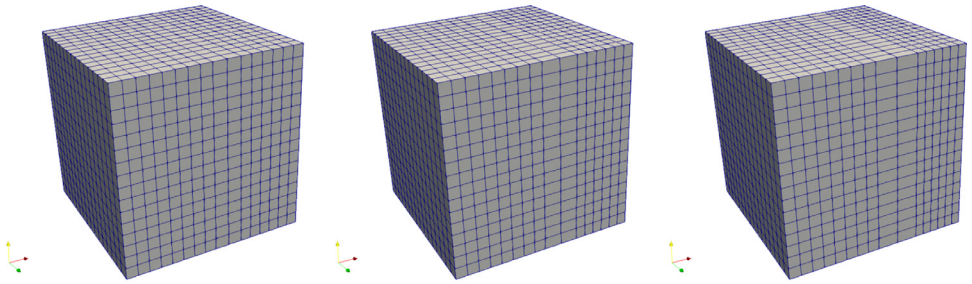

(a) ratio = 1.2 (b) ratio = 1.5 (c) ratio = 1.8

Fig. 12. The shape of the irregular elements. The overall domain consists of 512 elements.

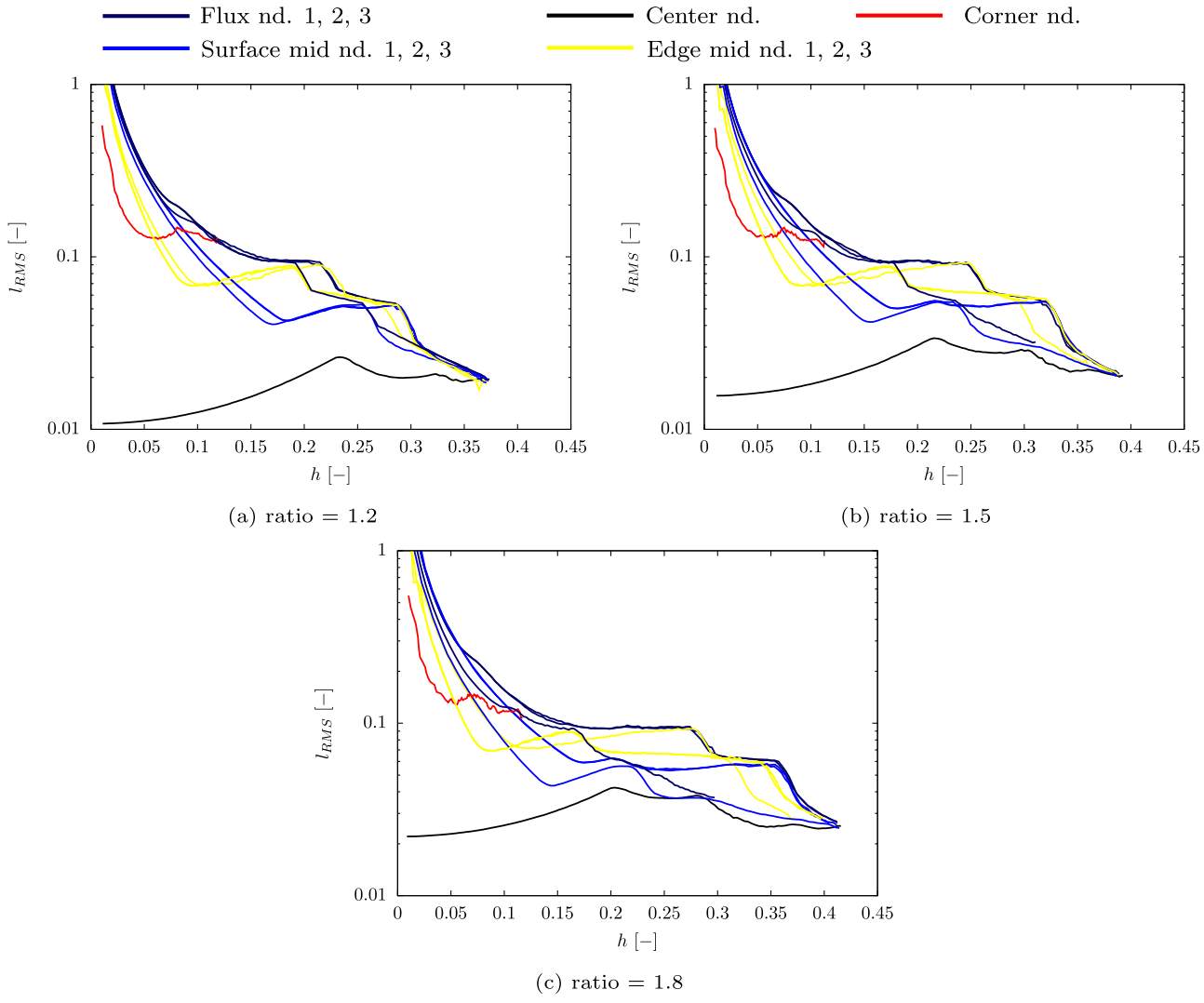

(a) ratio = 1.2 (b) ratio = 1.5

(c) ratio = 1.8

Fig. 13. Filtered results of the irregular meshes using BEM two-way coupling. The mesh node groups are retained for the irregular meshes with a difference that one representative of Flux, edge mid. and surface node groups has different characteristics. Since the element is a rectangle with squared base, there is for every mesh node group a pair with the same distances to the mesh source point. Thus, the reason is fully geometrical and connected with the mesh shape.

terpolation of the source in each element, it is sufficient to use the source term only for the source point that is at the center of the element (see Fig. 4). Thus, $\zeta_{e,i}$ in (15) is subject to the following conditions:

$$\zeta_{e,i} = \begin{cases} \zeta_{mp} & \text{if} \quad \vec{p}_j \in V_e \wedge \vec{\xi} = \vec{\xi}_{mp,e}, \\ 0, & \text{otherwise}, \end{cases} \tag{16}$$

where $\vec{\xi}_{mp,e}$ represents the position vector of the center source point of the given element. Integrating the element volume for the energy source contribution, we compute the value of the energy source introduced by the particle. For optional element e and particle j all of the $\zeta_{e,i}$ in (15) are zero except for the node in the center of the element. Thus we may write:

$$\sum_e \sum_i \sum_j \frac{1}{V_e} \int_\Omega \Phi_i \zeta_{e,i}(\vec{p}_j) \mathrm{d}\Omega. \Rightarrow \frac{\zeta_{\mathrm{mp}}}{\mathrm{V_e}} \int_\Omega \Phi_{\mathrm{mp}} \mathrm{d}\Omega = \zeta, \tag{17}$$

where ζ_{mp} is the source applied to the center node and Φ_{mp} the shape function for the center node which is computed as

$$\Phi_{mp} = [1-\chi^2][1-\eta^2][1-\psi^2] \tag{18}$$

with ψ, η and χ being the local isoparametric coordinates all with the same range of $[-1, 1]$. The value of ζ_{mp} is analytically computed as

$$\zeta_{mp} = \frac{\zeta V_e^g}{\int_\Omega \Phi_{mp} \mathrm{d}\Omega} = \zeta_{mp} = \frac{\zeta \cdot 8}{\int_{-1}^{1}[1-\chi^2][1-\eta^2][1-\psi^2]\mathrm{d}\chi\mathrm{d}\eta\mathrm{d}\psi} = \left(\frac{2}{3}\right)^3 \zeta, \tag{19}$$

where we denoted by $V_{c,e}^g$ the volume of the element in local coordinates.

As in Section 3.1, the remaining integrals in (15) may be computed in advance. We arrange them into matrices using (12) to obtain the final discrete version of Eq. (15):

$$[H]\{T\} = [G]\{q\} - [B]\left\{\beta_1 T - \beta_2 T^n + \beta_3 T^{n-1}\right\} + \sum_j \frac{\zeta}{V_e}\left[\frac{2}{3}\right]^3. \tag{20}$$

Equation (15) requires the calculation of the domain integral based on the particle presence and does not take into account the exact position of the particle. These two facts are considered disadvantages of the PIC method compared to the newly proposed BEM two-way coupling Algorithm in (11).

3.3. Numerical algorithm

We propose an algorithm for the hybrid BEM-PIC two-way coupling computations. The algorithm has the solution method as described in Algorithm 1.

In the step of searching for the nearest mesh node, we define to which mesh node group the nearest node belongs. The critical distance is specific for each of the five mesh node groups. We must therefore define five critical distances.

To facilitate the comparison of the results, we define the root mean square norm (RMS) as

$$l_{RMS} = \sqrt{\frac{\sum_{i=1}^{N}[T_{ana} - T_{num}]}{\sum_{i=1}^{N} T_{ana}^2}}, \tag{21}$$

where T_{ana} is analytical solution and T_{num} is the computational result using either BEM two-way coupling or PIC two-way coupling.

4. Definition of the critical distance

We consider a cubic domain $[0, 1]^3$ and place a particle in it that emits heat with a constant source ζ. Initially the domain is at $T = 0$. We prescribe Dirichlet boundary conditions on the boundary of the domain with the known analytical solution of this problem [35]:

$$T_{ana}(r, \tau) = \frac{\zeta}{4\pi r}\mathrm{erfc}\left(\frac{r}{2\sqrt{\tau}}\right), \tag{22}$$

where r is the Euclidean distance between the particle position and the selected node. The domain is meshed with cubic elements having quadratic interpolation for the functions and linear interpolation for the flux. Thus each element has 27 function nodes and 24 flux nodes. The integrals are approximated by Gaussian quadrature with 8 points. The number of Gauss quadrature points is chosen based on the analysis shown in Fig. 6b. Without loss of generality we place the particles in only (1/8)th of the element, because of symmetry (Fig. 5).

The time step is chosen according to the following analysis. We choose two particles with different locations and simulate them using different time steps as is represented in Fig. 6a. The results indicate that the choice $\tau = 10$ and $\Delta\tau = 1$ will ensure that the results of the simulations will not be affected by the time step.

The simulations are performed four times, twice for each of the two different mesh types. Firstly, we consider the mesh with regular elements and secondly a mesh with irregular, cuboidal elements. The distribution of the elements in the regular meshes is $4 \times 4 \times 4$, $8 \times 8 \times 8$ and $16 \times 16 \times 16$ with 64, 512 and 4096 elements respectively. The number of degrees of freedom for each of the meshes is 729, 4913 and 35,967 respectively. The analysis of irregularly shaped elements is performed for meshes with an $8 \times 8 \times 8$ distribution of elements. Each simulation is performed with only one particle within the domain. To obtain reliable results, we repeat the simulations for each mesh 10^5 times, changing only the position of the particle. The positions of the particles are defined using a geometry modeller - they are placed in 1/8th of the volume of a single element within the domain. The element does not share a side with the domain boundary. A constant dimensionless heat source of magnitude $\zeta = 10$ is specified for the particles.

4.1. Regular mesh

For each simulation the l_{RMS} and a distance d from the particle to the nearest source point ($\vec{\xi}$) are calculated. The distances can vary considerably depending on the mesh size, so we introduce a new dimensionless parameter that measures the distance between the particle and the mesh node,

$$h = \frac{d}{\sqrt[3]{V_e}}, \tag{23}$$

where V_e is the volume of the mesh element in which the particle is located. Depending on the type of mesh node closest to the particle position, the results can be divided into five mesh node groups with different properties (Fig. 7a). The first group (purple color) consists of all flux nodes, the second group (yellow) of the edge mid nodes, the third (blue) of the surface mid nodes, the fourth (red) of the corner node, and the last (black) of the center node. Each mesh node within the group exhibits similar properties, which are shown in Fig. 7b. On closer inspection, all three flux nodes exist within the purple group, and each of them separately has the same shape as the other two. Thus we have proved that the error in the calculated temperature is of the same order of magnitude at a given distance between particle and node, regardless of which mesh type of node is taken.

In Fig. 8 we show the relationship between l_{RMS} and the dimensionless distance for a set of particles that were located at an approximately equal distance from the edge mid mesh node. The inset panel shows that the l_{RMS} is highest for those particles for which the second closest mesh node is a flux node. Consider the l_{RMS} of the PIC method. While the PIC solution is constant for all particles within the same element, the analytical solution varies, since it depends on the particle position. Therefore the l_{RMS} of the PIC method will also have different values for the particles with different positions. Fig. 9b shows that the l_{RMS} of the PIC method have similar properties as the l_{RMS} obtained with the BEM two-way coupling algorithm.

Considering only the worst case simulations with the highest l_{RMS} values for two-way coupled BEM simulations and the lowest l_{RMS} for PIC two-way coupled simulations, we produced Fig. 10 using the data shown in Figs. 7 and 9. Without loss of generality, we select only one representative of the given node type group and apply a moving average filter to obtain a smooth relationship between l_{RMS} and distance.

The results show that for four groups of mesh nodes there is a point where the l_{RMS} results are the same for both PIC and the BEM coupled simulation. We mark this point as the critical distance $\hat{h}$, which is generally different for each node group. The corner node group, edge node group, flux node group, surface node group and center node group are given indexes a, b, c, d and e respectively. The center mesh node group is the only mesh node group that allows the particles in its vicinity to be calculated using the BEM two-way coupling algorithm without using the hybrid approach. This is due to the fact that the central nodes are domain nodes where the solution of the PDE is obtained explicitly from the known boundary values. The proposed critical distances for each node group are given in Table 1. The uncertainty in the critical distance is due to the small dependence of $\hat{h}$ on the mesh density. Additional in-

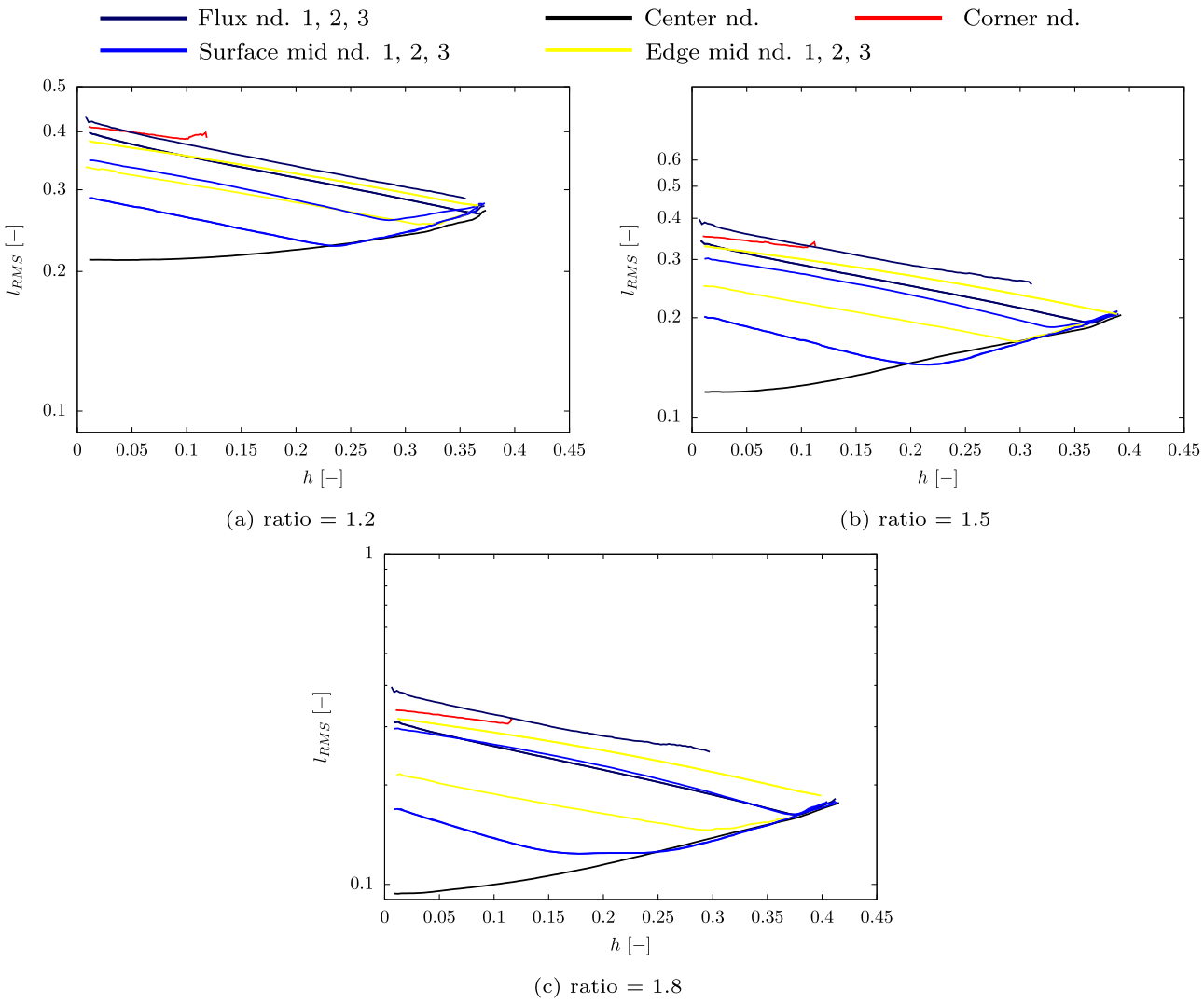

Fig. 14. Filtered results of the irregular meshes using PIC. Again, the mesh node groups are retained with one representative of every mesh node group having different characteristics due to the geometrical reasons.

Table 1
The proposed $\hat{h}$ values for the two-way coupled simulations when hybrid BEM-PIC approach is used.

Mesh node group	Proposed critical distance
$\hat{h}_a$	0.0225 ± 0.0025
$\hat{h}_b$	0.0425 ± 0.0025
$\hat{h}_c$	0.06 ± 0.005
$\hat{h}_d$	0.085 ± 0.005
$\hat{h}_e$	0

Table 2
The percentage of total volume for which the particles are computed with BEM V^A_{BEM} using the critical values $\hat{h}$ in Table 1 and the percentage of total volume, that was computed as a comparison of l_{RMS} values of BEM and PIC.

DOF	Mesh size	V^A_{BEM} [%]	V^C_{BEM} [%]
729	64	97.94	97.85
4913	512	98.24	98.36
35937	4096	97.86	98.16

formation about the relation of the BEM two-way coupling results versus the PIC two-way coupling results may be obtained from Fig. 11.

The same patterns on each panel suggest that the required distance between the mesh source point and a particle depends only on the mesh size. When the hybrid PIC-BEM approach is used, we want to investigate the contribution of the domain volume handled by the BEM two-way coupled algorithm and the contribution handled by the PIC two-way coupled algorithm. We calculate these contributions in two ways: V^A_{BEM} is calculated using the critical values $\hat{h}$ for each mesh node group, assuming that a critical distance represents the radius of a sphere with the center at the source point ξ. The sum of the volumes of the spheres for each ξ is equal to $V - V^A_{BEM}$. The second type of volume calculation is done by comparing the l_{RMS} value calculated with the BEM two-way coupling with the PIC two-way coupling for each particle. Since the number of particles is very large and evenly distributed in the volume, the simple count of particles handled by each type of two-way coupling algorithm gives a good indication of the volume. V^C_{RMS} is obtained by comparing the number of particles whose l_{RMS} computed with the BEM two-way coupling is lower than that of the PIC coupling (Table 2).

4.2. Irregular meshes

The two-way coupled simulations using the PIC two-way coupling and the BEM two-way coupling are also performed using irregular ele-

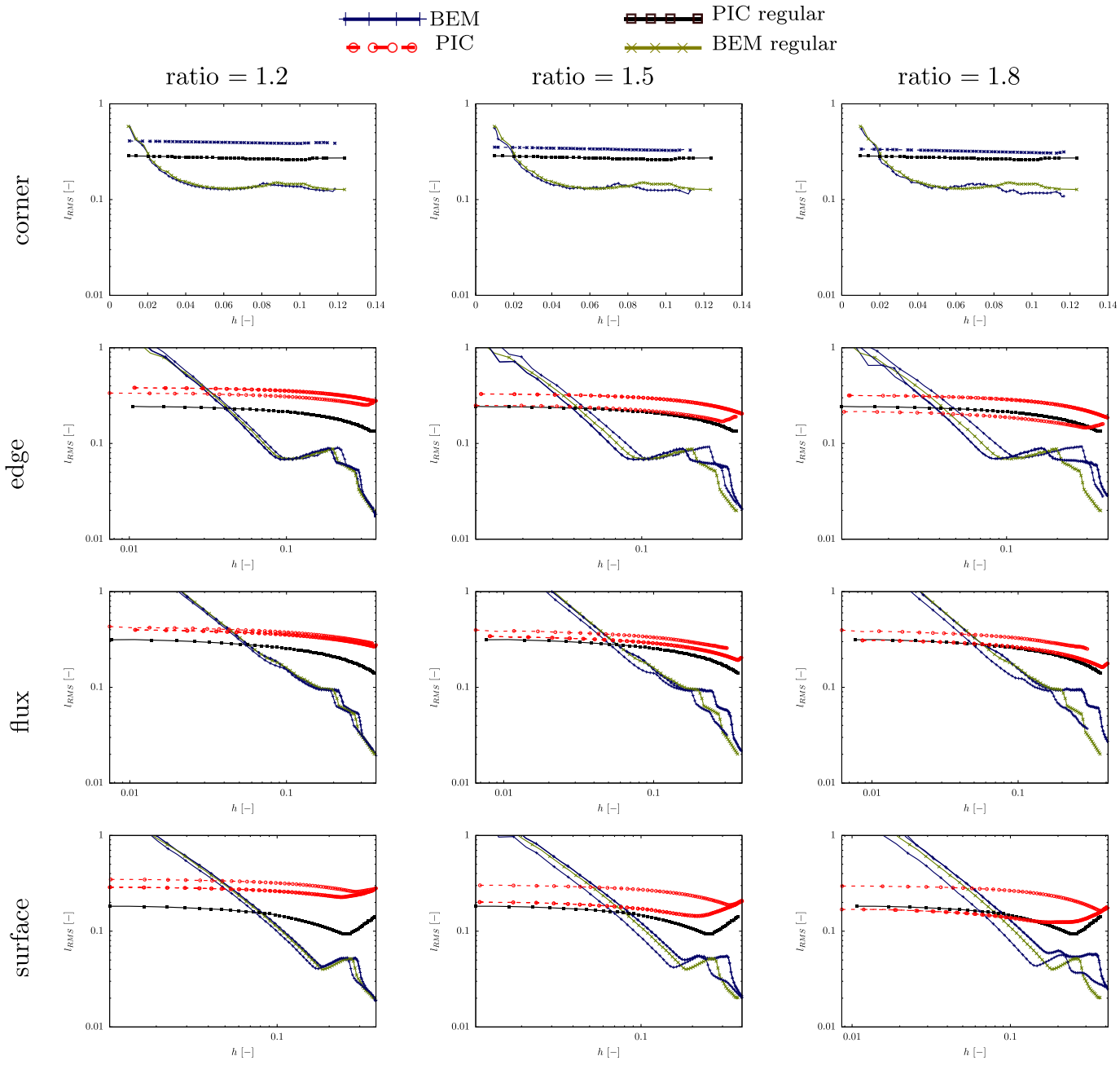

Fig. 15. The comparison of the results of a irregular mesh with the regular mesh for each mesh node group separately.

ments in the mesh. We used the same cuboidal domain $[0, 1]^3$ that was meshed with regular cubic and irregular cuboidal elements. The size of the mesh was $8 \times 8 \times 8$ with 512 elements. The particles are positioned inside the irregular element whose irregularity was implemented by stretching in the x direction. Only one layer of elements is stretched on the zy plane, which corresponds to 64 elements. So the base of the element is a square and the sides are rectangles, as shown in Fig. 12. We choose three cases with three different ratios between the x length and the zy length of the element. Since the element is longer in the x direction, the possible distance between the particle and the source point can be longer as we can see from Fig. 13b. Also, both PIC two-way coupling (Fig. 14) and BEM two-way coupling (Fig. 13) simulations show that the mesh node groups are retained with one representative from each group having different $l_{RMS}(h)$ dependencies, which is due to the mesh stretching in the x direction.

Table 3
The table shows the change of critical distance due to irregularities in the mesh elements.

Mesh node group	mesh type	ratio = 1.2	ratio = 1.5	ratio = 1.8
$\hat{h}_a$	Reg.	0.021	0.021	0.021
	Irr.	0.015	0.017	0.018
$\hat{h}_b$	Reg.	0.042	0.042	0.042
	Irr.	0.033	0.046	0.052
$\hat{h}_c$	Reg.	0.057	0.057	0.057
	Irr.	0.043	0.052	0.057
$\hat{h}_d$	Reg.	0.079	0.079	0.079
	Irr.	0.055	0.076	0.094

Further analysis of each mesh node group shows that the particle may have a smaller $\hat{h}$ for slightly distorted meshes, which becomes larger with more distorted meshes, as shown in Table 3. The table was created

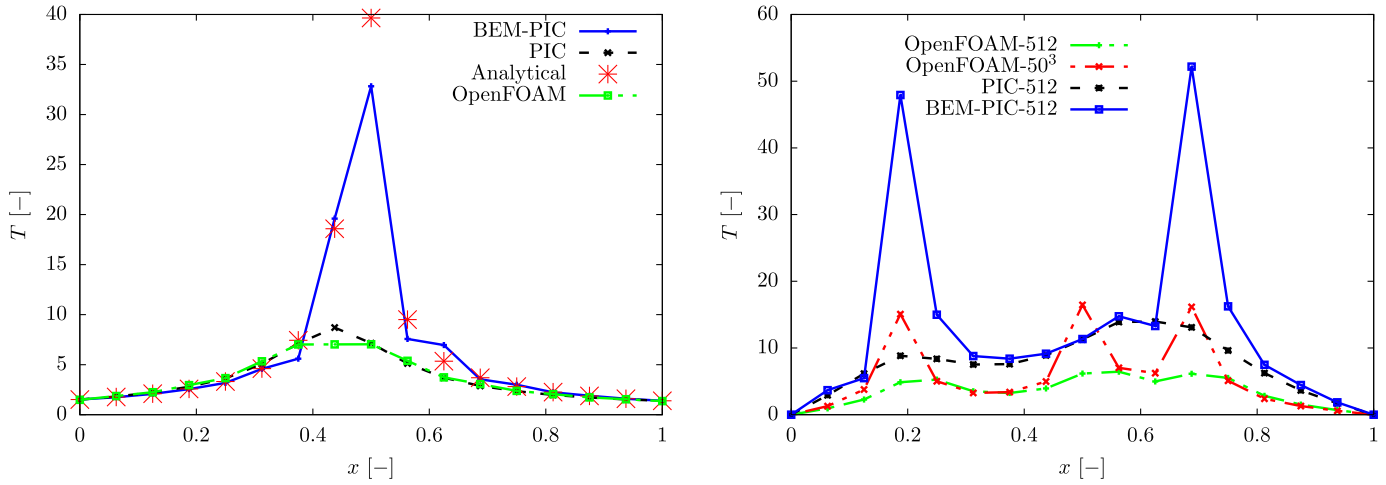

(a) 1 particle (b) Three particles

Fig. 16. The first case in 16 a includes one particle with the boundary conditions as given in Section 4. In the second simulation (16 b) we include three particles in the domain and change the boundary conditions. The temperature profiles are plotted over the same line for both of the cases (inlay panel in 16 a) with coordinates $P_1(0, 0.5, 0.5)$ and $P_2(1, 0.5, 0.5)$.

using the data presented in Fig. 15 . From the viewpoint of numerical methods, it is not advisable to use an even more distorted mesh. The results in Table 3 show that the critical distance $\hat{h}$ resulting from the regular meshes specified in Table 1 is conservative enough to be also used for meshes with distorted elements.

```
Initialize, compute the integrals in [H], ≤[G] and [B].
for every particle do
    Find the mesh element, in which the particle is located;
    Find the nearest mesh node;
end
while "current time" not equal to "end time" do
    Update the temperature field;
    for All nodes do
        if Node i is middle node then
            for All particles do
                if Particle j inside the parent element of node i
                AND the distanceto the nearest mesh node crosses
                the critical distance then
                    Add source term to the accumulation term
                    - equation (20);
                end
            end
        end
    end
    while "Convergence reached" do
        Setting RHS vector of equation (13) without sourcesum;
        for All particles i do
            if The distance from i-th particle to the nearest mesh
            node does not cross the critical distance then
                Add source to the RHS vector - equation (13);
            end
        end
        Check convergence: repeat steps until convergence is
        reached;
    end
end
Output results;
```

Algorithm 1: Hybrid BEM-PIC two-way coupling algorithm.

Table 4
Computed l_{RMS} values for the case represented in Fig. 16. The BEM-PIC represents the novel hybrid model, whose l_{RMS} are much better compared to the results obtained either with pure PIC (PIC in our code) or OpenFOAM.

Solver	l_{RMS}
hybrid BEM-PIC	0.162
PIC	0.736
OpenFOAM (PIC)	0.622

5. Numerical example

We calculate two cases of the same physical phenomenon as described in the above sections and compare the results with those obtained with the open source software code (OpenFOAM), which uses the PIC two-way coupling algorithm.

5.1. One particle

We simulate one particle, which is located inside the domain with size $[0, 1]^3$. The domain is prescribed with the same boundary conditions as in Section 4. The particle is located at $\vec{p} = (0.48, 0.48, 0.48)$, the time step is $\Delta\tau = 1$ with the end time $\tau = 10$. The results are shown in the Fig. 16a. As the particle is far enough away from the nearest mesh node (it does not cross the critical distance), it is coupled with the BEM method and its description of the temperature profile is by far most accurate in comparison to the analytical solution. We have calculated the same case using PIC coupling only of our solver and with OpenFOAM. The derivation of the two-way coupling with BEM is mathematically most correct, which is the reason for the better peak description. The coupling of our solver with PIC also has better peak description than OpenFOAM, which is due to interpolation implementation. OpenFOAM uses linear elements while our solver is based on quadratic elements. Since the analytical solution is known, we additionally calculate the l_{RMS} values (Table 4), which show that the novel two-way coupling algorithm describes the physical phenomenon much better.

5.2. Three particles

To verify the novel hybrid model algorithm, we perform a simulation with three particles in the same domain as in the previous

simulation. The positions of the particles are chosen so that one particle is closer to the mesh node than the critical distance $\hat{h}$. Additionally we change the boundary conditions. The surfaces $y = 0,\ y = 1,\ z = 0,\ z = 1$ are prescribed with zero gradient and the surfaces $x = 0,\ x = 1$ with temperature 0. The particles are positioned at $\vec{p}_1 = (0.2, 0.501, 0.501)$, $\vec{p}_2 = (0.7, 0.501, 0.501)$, $\vec{p}_3 = (0.501, 0.501, 0.501)$ with a dimensionless heat source of $\zeta = 10$. The results in Fig. 16b show that the new model describes the temperature peaks at the location of the particle significantly better and that a hybrid PIC-BEM two-way coupling algorithm is a good compromise between reliability and precision. Two of the particles have been far enough away from the nearest mesh node, while one crossed the critical distance. Therefore, two particles were computed using pure BEM coupling (two blue peaks) and one with PIC (small, blunt blue peak). Additionally we simulated the same case with only PIC coupling of our solver and also with OpenFOAM. Again, the proposed novel hybrid model describes the peaks much better, if the critical distance is not reached. The blunt blue peak represents the particle that has crossed critical distance and has been coupled using PIC. The peak is almost the same as if we used only PIC coupling for all particles (black line). The simulation performed using OpenFOAM with a denser mesh gives an indication of how many elements are needed to correctly describe the peaks of the temperature profile. The superiority of the novel hybrid model is due to its precise mathematical derivation. Its disadvantage is the hybrid tandem with the PIC method necessary to avoid the singularity. We have carried out the CPU time analysis for the case of three particles. Two of the particles have been computed using the BEM coupling method and one with the PIC. The wall time needed to calculate the given problem with the novel hybrid method is about $3.57\,s$. If only the PIC method is used as the coupling method, the solver needed about $4.33\,s$ to find the solution.

6. Conclusion

In this paper we present a novel two-way coupling model for the Euler-Lagrange simulation of particle-laden flows. The presented model uses the properties of the integral representation of the governing equations obtained via Green's theorem and the properties of the fundamental solution of the operator in the governing equation of the problem. The newly derived model is compared with the standard PIC model implemented in our in-house BEM code and with the open source code OpenFOAM. Through the comparison we discovered the existence of a critical distance between the particle and the mesh nodes where the new model outperforms the PIC model. Based on this information we proposed a new hybrid BEM-PIC two-way coupling model. Through numerous simulations we found that the critical distance depends only on the mesh and that irregularities in the mesh do not change the critical distance significantly. Additionally we present the values of the critical distance which should be used when the hybrid BEM-PIC is used for two-way coupled simulations. Finally, we performed two simulations to demonstrate the superiority of the novel two-way coupling algorithm over standard PIC implementation. The new algorithm outperforms other solvers in terms of accuracy.

Declaration of Competing Interest

The authors declare that they have no known competing financial interests or personal relationships that could have appeared to influence the work reported in this paper.

Acknowledgements

Ožbej Verhnjak acknowledges the financial support of the European Union European Regional Development Fund, and the Ministry of Education, Science and Sport of the Republic of Slovenia under the project Upgrading national research infrastructures HPC RIVR, implemented within the Operational Programme for the Implementation of the EU Cohesion Policy in the period 2014 -2020 (Contract No. C3330-18-952025).

The authors also thank the Deutsche Forschungsgemeinschaft for the financial support in the framework of the project STE544/58.

References

[1] van der Hoef M, van Sint Annaland M, Deen N, Kuipers J. Numerical simulation of dense gas-solid fluidized beds: a multiscale modeling strategy. Annu Rev Fluid Mech 2008;40(1):47–70. doi:10.1146/annurev.fluid.40.111406.102130.
[2] Ludwig W, Płuszka P. Euler-lagrange model of particles circulation in a spout-fluid bed apparatus for dry coating.. Powder Technol 2018;328:375–88.
[3] I Kolev N. Multiphase flow dynamics. 1: fundamentals. Multiphase Flow Dynamics 1 (Second Edition): Fundamentals 2005. doi:10.1007/b138144.
[4] Cui Y, Ravnik J, Hriberšek M, Steinmann P. Towards a unified shear-induced lift model for prolate spheroidal particles moving in arbitrary non-uniform flow. Computers & Fluids 2020;196:104323. doi:10.1016/j.compfluid.2019.104323. http://www.sciencedirect.com/science/article/pii/S004579301930283X
[5] Laín S, Sommerfeld M, Kussin J. Experimental studies and modelling of four-way coupling in particle-laden horizontal channel flow. Int J Heat Fluid Flow 2002;23(5):647–56. doi:10.1016/S0142-727X(02)00160-1.
[6] Anderson TB, Jackson R. Fluid mechanical description of fluidized beds. equations of motion. Industrial & Engineering Chemistry Fundamentals 1967;6(4):527–39. doi:10.1021/i160024a007.
[7] Enwald H, Peirano E, Almstedt A-E. Eulerian two-phase flow theory applied to fluidization. Int J Multiphase Flow 1996;22:21–66. doi:10.1016/S0301-9322(96)90004-X.
[8] Kaufmann A, Moreau M, Simonin O, Helie J. Comparison between lagrangian and mesoscopic eulerian modelling approaches for inertial particles suspended in decaying isotropic turbulence. J Comput Phys 2008;227(13):6448–72. doi:10.1016/j.jcp.2008.03.004.
[9] Traoré P, Laurentie J-C, Dascalescu L. An efficient 4 way coupling cfd-dem model for dense gas-solid particulate flows simulations. Computers & Fluids 2015;113:65–76. doi:10.1016/j.compfluid.2014.07.017. Small scale simulation of multiphase flows; http://www.sciencedirect.com/science/article/pii/S0045793014003028
[10] Zhou L, Yu Y, Cai F, Zeng Z. Two-phase turbulence models for simulating dense gas-particle flows. Particuology 2014;16:100–7. doi:10.1016/j.partic.2013.06.007.
[11] Ferry J, Balachandar S. A fast eulerian method for disperse two-phase flow. Int J Multiphase Flow 2001;27:1199–226. doi:10.1016/S0301-9322(00)00069-0.
[12] Crowe C, Schwarzkopf J, Sommerfeld M, Tsuji Y. Multiphase Flows with Droplets and Particles. Taylor & Francis; 1997. ISBN 9780849394690. https://books.google.si/books?id=CioXotlGMiYC
[13] Février P, Simonin O, Squires K. Partitioning of particle velocities in gas-solid turbulent flows into a continuous field and a spatially uncorrelated random distribution: theoretical formalism and numerical study. J Fluid Mech 2005;533:1–46. doi:10.1017/S0022112005004088.
[14] Elghobashi S. Particle-laden turbulent flows: direct simulation and closure models. Appl Sci Res 1991;48(3):301–14. doi:10.1007/BF02008202.
[15] Maxey MR. The gravitational settling of aerosol particles in homogeneous turbulence and random flow fields. J Fluid Mech 1987;174:441–65. doi:10.1017/S0022112087000193.
[16] Cundall PA, Strack ODL. A discrete numerical model for granular assemblies. Géotechnique 1979;29(1):47–65. doi:10.1680/geot.1979.29.1.47.
[17] Harlow FH. Hydrodynamic problems involving large fluid distortions. J ACM 1957;4(2):137–42. doi:10.1145/320868.320871.
[18] Crowe GT. REVIEW-Numerical Models for dilute gas-particle flows. Transactions of ASME 1982;104:297–303. doi:10.1115/1.3241835.
[19] Balachandar S, Eaton JK. Turbulent dispersed multiphase flow. Annu Rev Fluid Mech 2010;42(1):111–33. doi:10.1146/annurev.fluid.010908.165243.
[20] Capecelatro J, Desjardins O. An euler-lagrange strategy for simulating particle-laden flows. Journal of Computational Physics 2013;238:1–31. doi:10.1016/j.jcp.2012.12.015. http://www.sciencedirect.com/science/article/pii/S0021999112007462
[21] Liu K, Lakhote M, Balachandar S. Self-induced temperature correction for inter-phase heat transfer in euler-lagrange point-particle simulation. Journal of Computational Physics 2019;396:596–615. doi:10.1016/j.jcp.2019.06.069. http://www.sciencedirect.com/science/article/pii/S0021999119304772
[22] Balachandar S, Liu K, Lakhote M. Self-induced velocity correction for improved drag estimation in euler-Lagrange point-particle simulations. J Comput Phys 2019;376:160–85. doi:10.1016/j.jcp.2018.09.033.
[23] Gualtieri P, Picano F, Sardina G, Casciola CM. Exact regularized point particle method for multiphase flows in the two-way coupling regime. Journal of Fluid Mechanics 2015;773:520–61. doi:10.1017/jfm.2015.258. 1405.6969
[24] Ireland PJ, Desjardins O. Improving particle drag predictions in euler-Lagrange simulations with two-way coupling. J Comput Phys 2017;338:405–30. doi:10.1016/j.jcp.2017.02.070.
[25] Ravnik J, Škerget L, Žunič Z. Combined single domain and subdomain bem for 3D laminar viscous flow. Eng Anal Bound Elem 2009;33(3):420–4. doi:10.1016/j.enganabound.2008.06.006.
[26] Ravnik J, Škerget L, Žunič Z. Velocity-vorticity formulation for 3d natural convection in an inclined enclosure by bem. International Journal of Heat and Mass Transfer 2008;51(17):4517–27. doi:10.1016/j.ijheatmasstransfer.2008.01.018. http://www.sciencedirect.com/science/article/pii/S0017931008000719

[27] Kontoni D, Partridge P, Brebbia C. The dual reciprocity boundary element method for the eigenvalue analysis of helmholtz problems. Advances in Engineering Software and Workstations 1991;13(1):2–16. doi:10.1016/0961-3552(91)90040-B.
[28] Guo S, Wu Q, Li H, Gao K. Triple reciprocity method for unknown function's domain integral in boundary integral equation. Engineering Analysis with Boundary Elements 2020;113:170–80. doi:10.1016/j.enganabound.2019.12.014. http://www.sciencedirect.com/science/article/pii/S0955799719306757
[29] Guo S, Wu Q, Gu J, Wang W, Li X. An improved implementation of triple reciprocity boundary element method for three-dimensional steady state heat conduction problems. Engineering Analysis with Boundary Elements 2019;107:1–11. doi:10.1016/j.enganabound.2019.06.013. http://www.sciencedirect.com/science/article/pii/S0955799719302449
[30] Tibaut J, Ravnik J. Fast boundary-domain integral method for heat transfer simulations. Engineering Analysis with Boundary Elements 2019;99:222–32. doi:10.1016/j.enganabound.2018.12.003. http://www.sciencedirect.com/science/article/pii/S0955799718304776
[31] Gaul L, Kögl M, Wagner M. Boundary Element Methods for Engineers and Scientists: An Introductory Course with Advanced Topics. Springer Berlin Heidelberg; 2013. ISBN 9783662051368. https://books.google.si/books?id=RZnsCAAAQBAJ
[32] Niliot CL. The boundary-element method for the time-varying strength estimation of point heat sources: application to a two-dimensional diffusion system. Numerical Heat Transfer, Part B: Fundamentals 1998;33(3):301–21. doi:10.1080/10407799808915035.
[33] Wrobel LC, Aliabadi M. The Boundary Element Method, Applications in Thermo-Fluids and Acoustics. Wiley; 2002. ISBN 9780471720393. https://books.google.si/books?id=2uFIAQAAIAAJ
[34] Ravnik J, Škerget L. Integral equation formulation of an unsteady diffusion-convection equation with variable coefficient and velocity. Computers & Mathematics with Applications 2014;66(12):2477–88. doi:10.1016/j.camwa.2013.09.021. http://www.sciencedirect.com/science/article/pii/S0898122113005889
[35] Carslaw H, Jaeger J. Conduction of Heat in Solids. Clarendon Press; 1986. ISBN 9780198533689. https://books.google.si/books?id=y20sAAAAYAAJ